ARL-TR-8922 • MAR 2020

DEVCOM ARMY RESEARCH LABORATORY

Method and Development of an In-Situ, Optical Measurement of Shock Demagnetization in Single-Crystal Ferrimagnets

by Brian L Wilmer, Steven W Dean, Jennifer L Gottfried, W Casey Uhlig, and JU Cazamias

NOTICES

Disclaimers

The findings in this report are not to be construed as an official Department of the Army position unless so designated by other authorized documents.

Citation of manufacturer's or trade names does not constitute an official endorsement or approval of the use thereof.

Destroy this report when it is no longer needed. Do not return it to the originator.

ARL-TR-8922 ● MAR 2020

Method and Development of an In-Situ, Optical Measurement of Shock Demagnetization in Single-Crystal Ferrimagnets

Brian L Wilmer
SURVICE Engineering Company, Belcamp, MD

Steven W Dean, Jennifer L Gottfried, W Casey Uhlig, and JU Cazamias
Weapons and Materials Research Directorate, CCDC Army Research Laboratory

REPORT DOCUMENTATION PAGE

Form Approved
OMB No. 0704-0188

1. REPORT DATE *(DD-MM-YYYY)*	2. REPORT TYPE	3. DATES COVERED (From - To)
March 2020	Technical Report	1 July 2018–1 July 2019

4. TITLE AND SUBTITLE
Method and Development of an In-Situ, Optical Measurement of Shock Demagnetization in Single-Crystal Ferrimagnets

5a. CONTRACT NUMBER

5b. GRANT NUMBER

5c. PROGRAM ELEMENT NUMBER

6. AUTHOR(S)
Brian L Wilmer, Steven W Dean, Jennifer L Gottfried, W Casey Uhlig, and JU Cazamias

5d. PROJECT NUMBER

5e. TASK NUMBER

5f. WORK UNIT NUMBER

7. PERFORMING ORGANIZATION NAME(S) AND ADDRESS(ES)
CCDC Army Research Laboratory
ATTN: FCDD-RLW-PA
Aberdeen Proving Ground, MD 21005

8. PERFORMING ORGANIZATION REPORT NUMBER
ARL-TR-8922

9. SPONSORING/MONITORING AGENCY NAME(S) AND ADDRESS(ES)

10. SPONSOR/MONITOR'S ACRONYM(S)

11. SPONSOR/MONITOR'S REPORT NUMBER(S)

12. DISTRIBUTION/AVAILABILITY STATEMENT
Approved for public release; distribution is unlimited.

13. SUPPLEMENTARY NOTES
ORCID IDs: Jennifer L Gottfried, 0000-0002-1282-1928; W Casey Uhlig, 0000-0003-1815-0106

14. ABSTRACT
Magnetic behavior coupled to the rapid dynamics of shock is relatively unexplored and warrants further investigation. This work reports on the development of an all-optical magnetization detection system, capable of resolving changes in the magnetic landscape on impact-relevant timescales. Classical demagnetization measurements are inherently bulk, providing little to no direct microscopic information. Optical techniques provide a wealth of rich information and have yet to be applied to the complicated dynamic magnetic landscape during shock. Magnetized materials exhibit circular birefringence, which modifies the polarization state of reflected and transmitted light. As a result, linearly polarized light propagating through the magnetized material is rotated, known as Faraday rotation. This change is a direct measurement of the degree and direction of the magnetization through which the light propagated. As we seek novel applications exploiting electromagnetism, understanding the magneto-mechanics physics will become increasingly important. To that end, we designed and built a setup to measure Faraday rotation of a 780-nm probe laser passed through single-crystal yttrium iron garnet during impact of laser-induced shock waves.

15. SUBJECT TERMS
Faraday rotation, magnetism, yttrium iron garnet, YIG, shock demagnetization, laser-induced breakdown, magnetic domain

16. SECURITY CLASSIFICATION OF:			17. LIMITATION OF ABSTRACT	18. NUMBER OF PAGES	19a. NAME OF RESPONSIBLE PERSON
a. REPORT	b. ABSTRACT	c. THIS PAGE			Brian L Wilmer
Unclassified	Unclassified	Unclassified	UU	28	19b. TELEPHONE NUMBER (Include area code) (410) 278-7315

Contents

List of Figures iv

1. Introduction 1

2. Fundamental Magnetism Background 1

3. Shock Demagnetization Background 2

4. Optical Background 5

5. Experimental Approach 6

6. Results 14

7. Conclusion 17

8. References 18

List of Symbols, Abbreviations, and Acronyms 20

Distribution List 21

List of Figures

Fig. 1 Examples of magnetic ordering: unaligned domains, domains aligned by applying a magnetic field, and ferrimagnetic ordering 2

Fig. 2 Typical bulk, shock-demagnetization experimental scheme 2

Fig. 3 Oscilloscope trace of shock-induced demagnetization in YIG. Periodicity corresponds to reverberation of stress wave in the YIG platelet. 4

Fig. 4 Experimental and theoretical magnetization curves for two shock-induced strain fields. Smooth curves correspond to independent grain theory. Curves with slope discontinuity correspond to interacting grain theory. 5

Fig. 5 Schematic representation of linearly polarized light incident on a polarization analyzer, with incident intensity I_o and angular mismatch θ between incident and transmitted polarization axes 6

Fig. 6 Single-crystal YIG sample—5.75 mm diameter and 0.35 mm thick—shown attached to aluminum sample mount with charring due to laser-induced plasma damage, and unmounted (inset) 7

Fig. 7 Absorption spectrum of YIG 7

Fig. 8 Faraday rotation geometry and shock direction 8

Fig. 9 Shock demagnetization experimental setup with lenses L1-L3, mirrors M1-M5, polarizing prisms P1-P2, detectors DET1-DET3, bandpass filters BF1-3, magnet, sample, and lasers 9

Fig. 10 Realization of experimental setup in Fig. 9 9

Fig. 11 a) Electromagnet used to supply external field; b) electromagnetic cores used to extend and homogenize the magnetic field 10

Fig. 12 Cross section of magnetic field about 6.35 mm away from face of magnet with no core (left); scan direction (right). Vertical lines indicate core edges. 11

Fig. 13 Magnetic field cross sections from a) 4140 steel vs. mild steel, b) 4140 steel with a 3.175-mm hole, and c) tapered vs. solid electromagnet cores. Vertical lines indicate core edges. 11

Fig. 14 3-D plot of magnetic field map from 4140 steel core with a 3.175-mm bored hole for laser clearance 12

Fig. 15 Circuit diagram and realization of high-speed detectors 13

Fig. 16 Observed bandwidth of Si, PIN-diode based detectors as measured by sinusoidally modulating laser input intensity 14

Fig. 17 Probe laser intensity transmitted through the analyzer rotated to a) 20° and b) 21° away from crossed as the applied external field is ramped up. Insets zoomed in on low-intensity tails. 15

Fig. 18 Signal from YIG in 0.13 T magnetic field and air shock..... 16
Fig. 19 a) Signal and b) pickoff detector signals during laser-induced breakdown air shock (no sample) 16
Fig. 20 Effect of shielding the laser-beam path from air-pressure fluctuations generated by laser-induced breakdown in air 17

1. Introduction

The US Army Combat Capabilities Development Command Army Research Laboratory has a long history of studying novel materials and their full range of behavior in various impact scenarios. A relatively underexplored area is the magnetic behavior before, during, and after such events. The magnetic behavior of a material is determined by its crystal and electronic structure. Unlike many macroscopic mechanical properties (bulk and shear moduli, elastic constants, etc.), the macroscopic magnetic behavior is comparatively well understood and predicted by solid-state physics. However, when coupled with the rapid dynamics of shock events, it is not well described and warrants further investigation. As we seek novel applications exploiting electromagnetism, understanding the magneto-mechanics physics will become increasingly important. This work reports on the development of an all-optical magnetization detection system, capable of resolving changes in the magnetic landscape on impact-relevant timescales.

2. Fundamental Magnetism Background

The fundamental unit of magnetism is the magnetic dipole resulting from the spin of an electron. In an atom or molecule, electrons fill lower orbitals coupling spin up to spin down, leaving no net magnetic moment. The outermost orbital, frequently only partially filled, leaves the opportunity for unpaired spins and thus magnetism. Furthermore, the electronic ordering of some materials is such that it is energetically favorable to have multiple unpaired spins even with an even number of outer electrons. These unpaired spins bind together forming domains, small microscopic regions of a singular spin species.

How these domains align, whether spontaneously or when placed in a magnetic field, determines whether a material is categorically ferromagnetic, antiferromagnetic, paramagnetic, or ferrimagnetic. When the domains align, a material is said to be “magnetized”. A ferromagnetic material will become magnetized in an applied field and maintain that magnetization when the field is removed. An antiferromagnetic material will not magnetize, as the neighboring magnetic domains align antiparallel leaving no net magnetic moment. Paramagnetic materials will weakly magnetize in an applied field, but will not maintain that order when the field is removed. Ferrimagnetic materials are weak ferromagnets. Like antiferromagnetism, their domains align antiparallel. However, they have unequal magnetic moments leaving a small residual magnetization (Fig. 1).

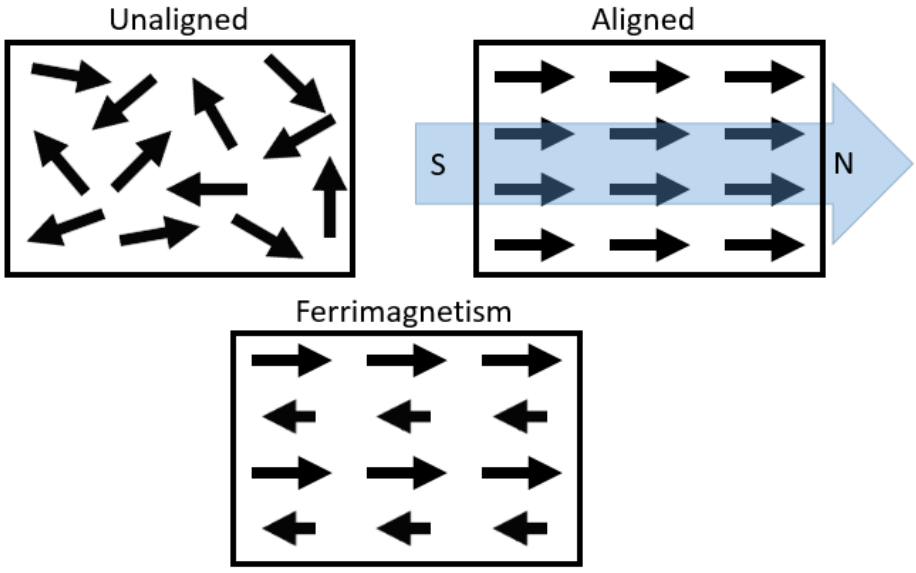

Fig. 1 Examples of magnetic ordering: unaligned domains, domains aligned by applying a magnetic field, and ferrimagnetic ordering

3. Shock Demagnetization Background

This work studies magnetic domain size and dynamics during shock loading. Magnetized materials can lose their magnetization when the crystal structure is strongly and quickly perturbed. This behavior is known as shock demagnetization. Shock demagnetization has been studied for applications in pulsed power,[1–4] where a rapid change of a strong magnetic field induces large currents in nearby conducting loops. In a typical demagnetization experiment, explosives or impactors shock a sample that is wrapped with pickup coils, allowing the time-dependent induced voltage to be recorded (Fig. 2). If necessary, an external magnetic field can be applied during the impact.

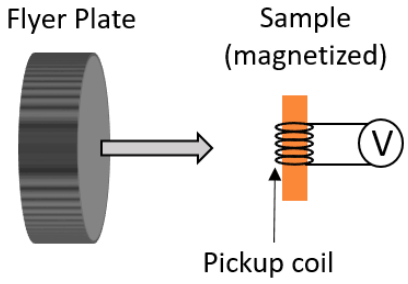

Fig. 2 Typical bulk, shock-demagnetization experimental scheme

These measurement types are inherently bulk, integrating the entire volume enclosed by the pickup coil into a single trace. Optical techniques capable of yielding a variety of rich information have yet to be fully utilized in these

experiments. Optical measurements of magnetization provide multidimensional microscopic information and are noninvasive, as no physical contact is necessary with a sample.

Early work by Dennis Grady made significant progress into the experimental methods and theoretical description of shock demagnetization. The mechanism is the induced shock anisotropy, which overcomes the natural magnetic ordering (anisotropy).[5–7] Grady derived expressions for the contributions to the thermodynamic energy and minimized them to predict magnetization dynamics. The contributions to the total thermodynamic energy, E, are

$$E_H + E_{me} + E_{s/d} + E_{ex} + E_k,$$

where E_H is interaction energy between the magnetic domains and the applied external magnetic field, E_{me} is the magnetoelastic energy and source of shock demagnetization, and $E_{s/d}$ is the self/demagnetizing energy. E_{ex} is the ferromagnetic exchange energy, which is a consequence of the spatial overlap of the atoms' charge distributions in a material and the Pauli exclusion principle. Since electrons cannot occupy the same orbital while having the same spin, these electrons must be spatially farther apart. The exchange energy is minimized (maximized) for parallel (antiparallel) spins. However, the more antiparallel interacting electrons' spins are, the spatially closer they are allowed to be, ultimately limited by coulomb repulsion. This interaction is fundamental to generating ferromagnetism. The fifth and final term, E_k, is due to the crystal anisotropy. It is 10–30 times weaker than the shock-induced anisotropy in magnetic materials, and can be neglected.

Assuming the applied field and magnetization are orthogonal, explicit expressions for these terms are

$$E_H = -\vec{H}_e \cdot \vec{M}_s = -H_e M_s \cos\theta$$

$$E_{me} = be \sin^2\theta$$

$$E_{s/d} = -\frac{1}{2}\vec{H}_d \cdot \vec{M}_s = +1.1\frac{D}{L}M_S^2 \sin\theta$$

$$E_{ex} = \frac{8}{D}\sqrt{Abe}\sin^2\theta$$

where H_e is the externally applied magnetic field, M_s the saturation magnetization, θ the angle between the magnetization and the applied field, b the magnetoelastic constant, e the strain, H_d the demagnetizing field generated by the domains that seek to de-align them, D the domain width, L the sample thickness, and A the exchange energy constant.

The increase in magneto-elastic energy resulting from shock brings the system out of its equilibrium domain configuration. The domains fracture and change spin orientation to minimize the total energy. The self-energy and the exchange energy are the only domain-wall-dependent terms. Thus, minimizing the total energy with respect to D yields the predicted domain width during shock:

$$D = \left[\frac{8L(A|be|)^{1/2}}{1.1M_S^2}\right]^{1/2}.$$

In the ferrimagnet yttrium iron garnet (YIG), with A =3 pJ/m, b = 0.35 J/m^3, and M_S = 0.134 T, Grady estimated that a 1-mm-thick crystal with a strain of e = –0.01 in the <100> direction generates a 20-μm fractured domain width. Contemporary experimental techniques of the time were unable to test this prediction.

Bulk measurements could be done, however, and Fig. 3 shows a representative trace reproduced from Grady et al.[6] produced via a shock demagnetization experiment using the scheme in Fig. 2. Because an external magnetic field was applied to YIG, magnetic ordering returns after the shock passes. Thus, the oscillations are due to cycles of demagnetization and remagnetization corresponding to successive passage and reflection of the shock wave.

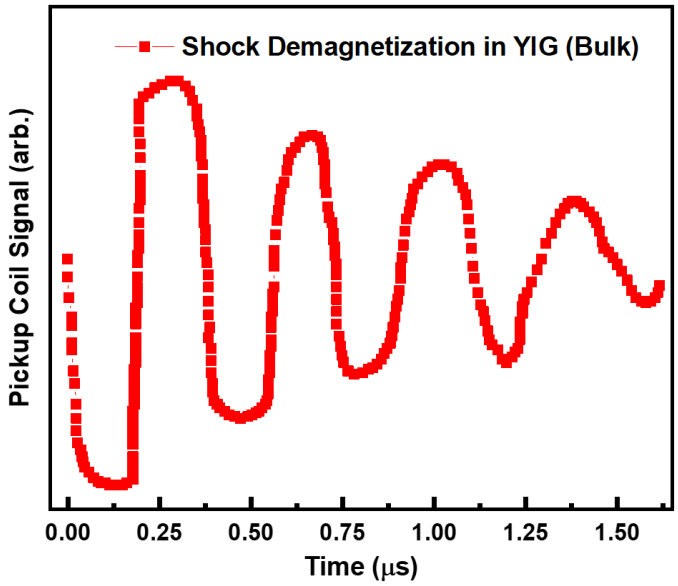

Fig. 3 Oscilloscope trace of shock-induced demagnetization in YIG. Periodicity corresponds to reverberation of stress wave in the YIG platelet.

The theoretical and experimental data from Grady relating the amount of shock demagnetization as a function of external magnetizing field and shock-induced strain is shown in Fig. 4.[6] His data supported the hypothesis that the magnetic grains

(microscopic single crystals, consisting of multiple magnetic domains) reorder independently in polycrystalline materials.

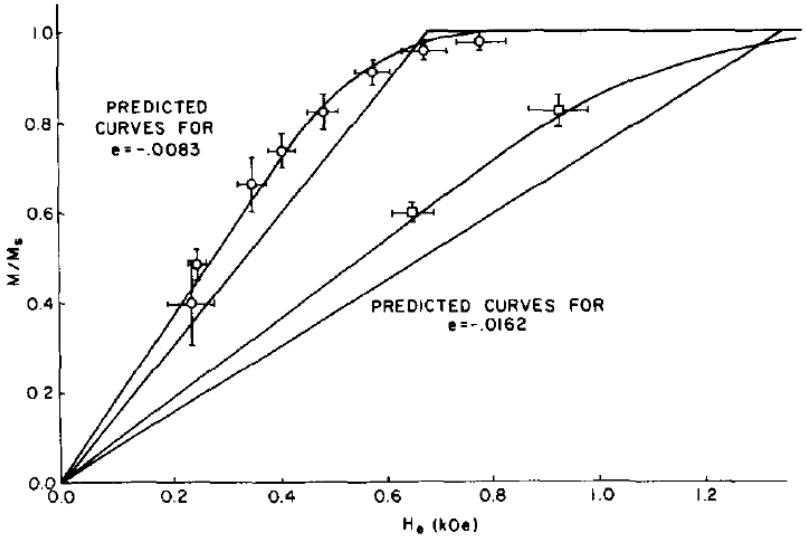

Fig. 4 Experimental and theoretical magnetization curves for two shock-induced strain fields. Smooth curves correspond to independent grain theory. Curves with slope discontinuity correspond to interacting grain theory.

Grady also predicted and observed that the rise time of the induced voltage from demagnetization was comparable to the strain rate, that is, the magnetization responds simultaneously to the change in mechanical structure during shock experiments. Thus, measurements of the magnetization also serve as a mechanical diagnostic of a material under shock loading.

4. Optical Background

Optical magnetization measurements can be either transmissive or reflective. This work uses Faraday rotation, a magneto-optical effect in transmissive materials. By focusing laser light through the sample with a beam diameter on the order of the predicted domain size, we are able to measure the magnetization on length and timescales appropriate to Grady's predictions.

Faraday rotation was first discovered by Michael Faraday in 1845. Light propagating through a magnetic medium experiences a circular birefringence where the left and right polarized light components remain in phase, resulting in rotation of the linear polarization state of the propagating light. This effect is wavelength and temperature dependent and can be quite large, on the order of thousands of degrees per centimeter, and is about 600 deg/cm in YIG at room temperature at

780 nm.[8,9] As a result of the large magnitude, it is easily measurable with conventional polarizers.

Many materials exhibit Faraday rotation and this is characterized by the degree of rotation per unit length at saturation magnetization. Maximum Faraday rotation is achieved when a sufficiently strong magnetic field is applied to a material as to saturate its magnetization.

To experimentally measure Faraday rotation, one propagates light with known intensity and linear polarization through a magnetized material and analyzes the resultant light with a polarizer. Malus' law for polarizers correlates the observed intensity to the rotation angle. Given an angular mismatch θ between the transmission axis of a polarizer and the incident light's axis of polarization, the transmitted light is polarized along the transmission axis of the analyzer and its intensity reduced by $cos^2\theta$ (Fig. 5). Unpolarized light experiences a 50% intensity reduction when passed through a linear polarizer.

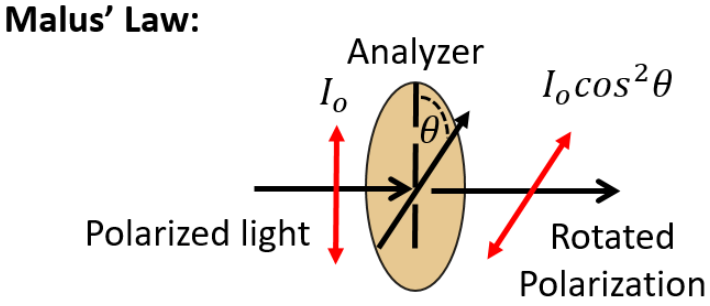

Fig. 5 Schematic representation of linearly polarized light incident on a polarization analyzer, with incident intensity I_o and angular mismatch θ between incident and transmitted polarization axes

5. Experimental Approach

A single-crystal YIG disk, 5.75 mm in diameter by 0.35 mm thick, was investigated as shown in Fig. 6 (and in front of the magnet in Fig. 11a).

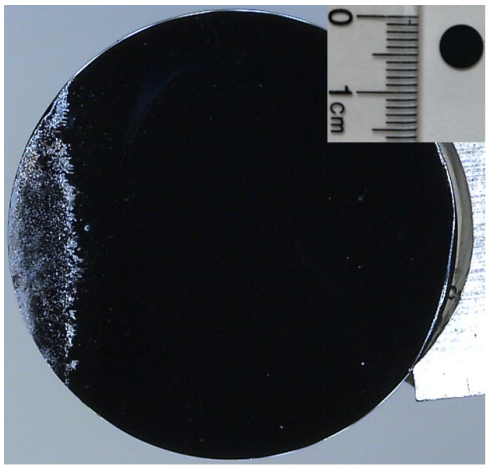

Fig. 6 Single-crystal YIG sample—5.75 mm diameter and 0.35 mm thick—shown attached to aluminum sample mount with charring due to laser-induced plasma damage, and unmounted (inset)

It is grown in the <111> direction, which is also the easy-axis of magnetization, its preferred magnetic anisotropy axis along which it magnetizes. It is a ferrimagnet that saturates at 0.14–0.17 T and has a remnant magnetization of less than 2.51 μT.[10,11] The absorption spectrum of bulk YIG is shown in Fig. 7, adapted from Wemple et al.[12] Strong absorption prevents transmission measurements in the visible and most of the near-infrared (NIR) spectrum. However, a window near 760–820 nm, where the absorption coefficient drops below 100 cm^{-1}, allows 3% to 6% transmission for our 0.35-mm sample.

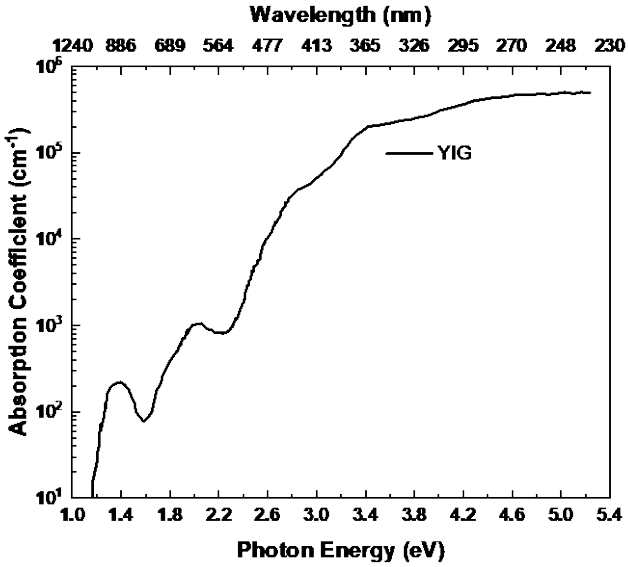

Fig. 7 Absorption spectrum of YIG

To maximize the Faraday rotation, the wave vector of the laser light must be parallel to the magnetization. To generate maximum demagnetization, the sample must be magnetized orthogonally to the propagation direction of the shock wave. The strain field from the shock wave then dominates the crystal's natural ordering 90° from the initial magnetic anisotropy axis. This geometry is shown in Fig. 8. Since the sample has little remnant magnetization, an externally applied field is necessary during measurements.

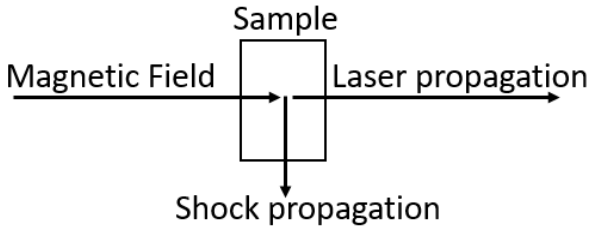

Fig. 8 Faraday rotation geometry and shock direction

The light source is a current- and temperature-controlled diode laser system (Thorlabs TED200C, LDC205C, and LDM56 [Thorlabs, Inc., Newton, New Jersey]), providing current stable to within 1.5-μA drift over 24 h. A continuous wave 0–10 mW laser diode with a wavelength of 780 nm was chosen to minimize absorptive loses in the NIR while also being able to use available silicon (Si)-based detectors.

The experimental setup optical diagram is shown in Fig. 9 and the realization in Fig. 10. A laser-induced shock was applied with a 1064-nm neodymium-doped yttrium aluminum garnet (Nd:YAG) laser (6-ns pulse width, 850-mJ maximum energy per pulse) on and near the edge of the YIG disk. The focused Nd:YAG pulse results in ionization and breakdown of the ambient air (or YIG disk), forming a dense, hot microplasma, which subsequently generates a shock wave that transmits into the surrounding medium (air or YIG). The focal position of the laser determines whether the breakdown occurs in the air or directly on the sample. The latter results in increased shock transmission and shock intensity as there is no air gap between the plasma and sample (i.e., the laser-induced shock wave rapidly decreases in intensity and velocity with increasing distance from the laser focus). The probe laser for Faraday rotation was directed through the sample's center to minimize complications arising from shock wave reflections at the sample's edge.

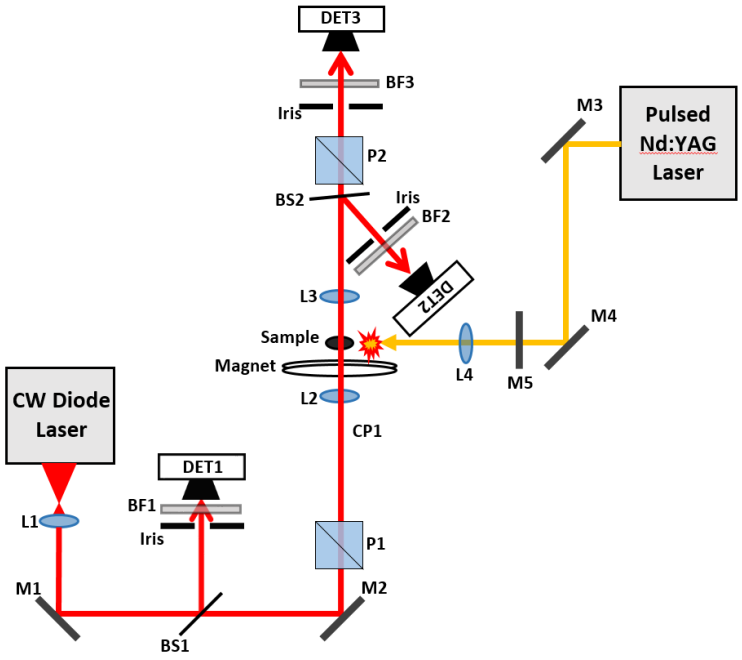

Fig. 9 Shock demagnetization experimental setup with lenses L1-L3, mirrors M1-M5, polarizing prisms P1-P2, detectors DET1-DET3, bandpass filters BF1-3, magnet, sample, and lasers

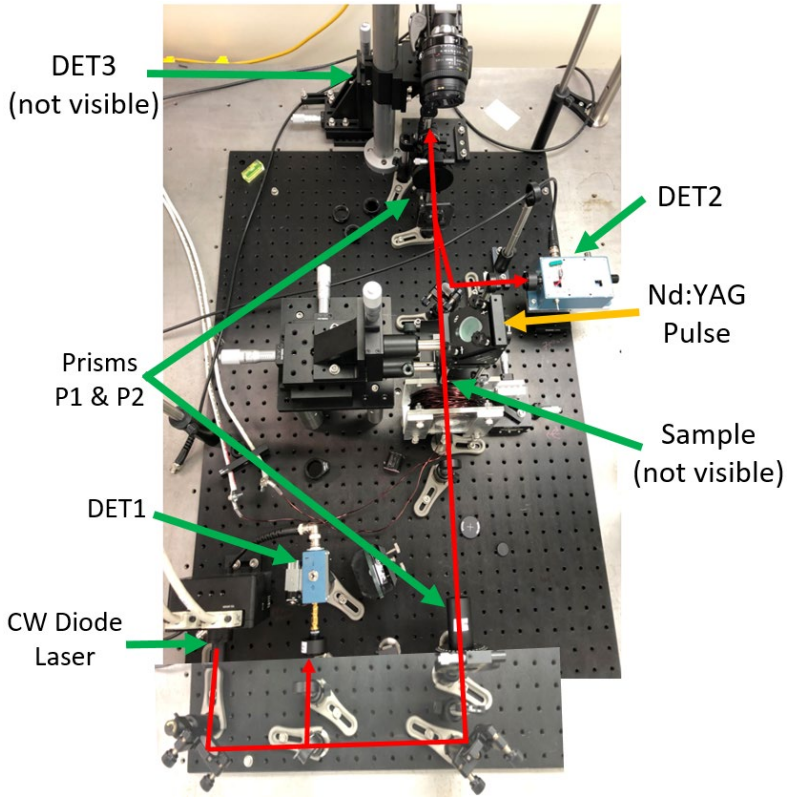

Fig. 10 Realization of experimental setup in Fig. 9

A 15-mm focal length (FL) lens collimates the diode's emission, which then passes through a Glan–Thomson prism with a 10^6 extinction ratio to generate a high-purity, linear polarization state. A 1× telescope consisting of a pair of 100-mm FL lenses focuses the 3-mm-diameter diode laser beam to a 30-μm spot size on the sample. The 780-nm light transmitted through the sample is re-collimated and a high-speed detector records the light intensity analyzed by a second polarizing prism.

A pair of fused silica windows serve as two pickoff beam splitters to monitor the probe laser intensity before and directly after the sample. This allows for discrimination and correction for any variations in the measured intensity after the analyzer due to laser fluctuations, mechanical sample motion, or other nonpolarization-related behavior.

The electromagnet constructed for these measurements is shown in Fig. 11 and generates fields at about 4.41 mT/A. It consists of 300 turns of square cross-section 14 AWG magnet wire, with a total resistance of 0.42 Ω, a 25.4 mm diameter center opening, 101.6 mm outer diameter, and 25.4 mm depth. Current is supplied by an Agilent N5764A unipolar power supply (21 V, 75 A) (Agilent Technologies, Santa Clara, California). At maximum output, it is capable of generating a 0.2 T field in the magnet center. Due to the experimental geometry, to receive the shock the sample must reside outside of the magnet, where the field decays (at one magnet radius the field drops ~50%) and becomes less homogeneous. Gradients in the applied magnetic field would result in gradients in the sample's magnetic landscape, complicating the domain structure and dynamics. The electromagnet is also unable to generate a saturating field (0.14 T for YIG) externally due to the power supply's upper-voltage limit.

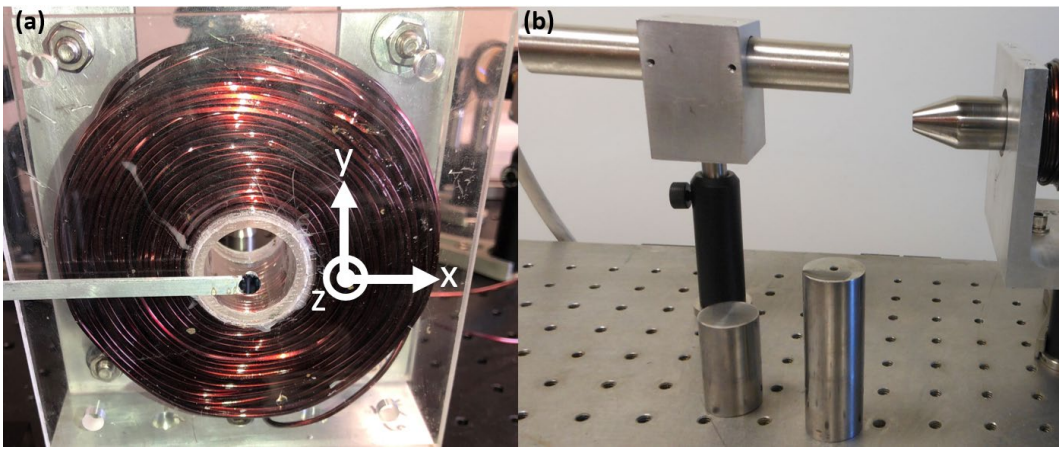

Fig. 11 a) Electromagnet used to supply external field; b) electromagnetic cores used to extend and homogenize the magnetic field

A solution to extend and homogenize the field to some degree is to use a ferromagnetic core, also commonly employed to increase an electromagnet's output and reduce current consumption. To this end, cores were constructed from steel alloys in different geometries (shown in Fig. 11b). The cores were all 25 mm diameter to easily slide inside the magnet and 76 mm overall length. Additional solid lengths were constructed to be daisy-changed, as longer cores collect more magnetic field lines. The 4140 steel variants were 1) a solid core with no tapered surface, 2) a solid core with a 21° taper to a 10-mm flat face, and 3) a core with a 3.175-mm bored hole. The hole was necessary for probe laser beam clearance. A fourth core consisted of solid mild steel. Their effect on the field was probed with a Hall probe while the magnet current was held constant at 2 A.

Figure 12 shows a cross section of the field from the magnet with no core (air) about 6.35 mm in the Z (axial) direction from the magnet face (the closest approach possible because of the magnet's 6.35 mm acrylic confinement). Figure 13 shows the resulting field for the various cores at multiple standoff distances from the core surface with the core extended various distances X (mm) from the magnet surface.

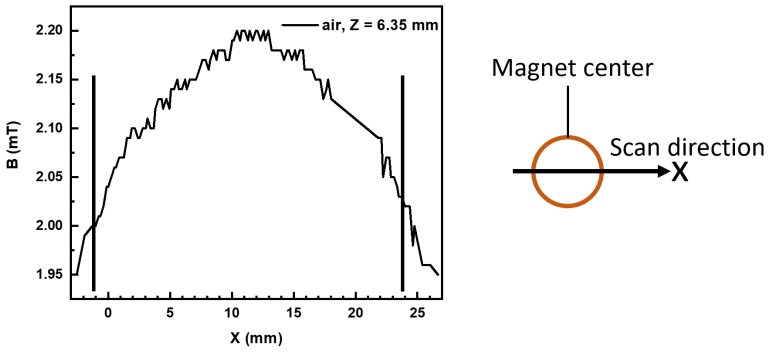

Fig. 12 Cross section of magnetic field about 6.35 mm away from face of magnet with no core (left); scan direction (right). Vertical lines indicate core edges.

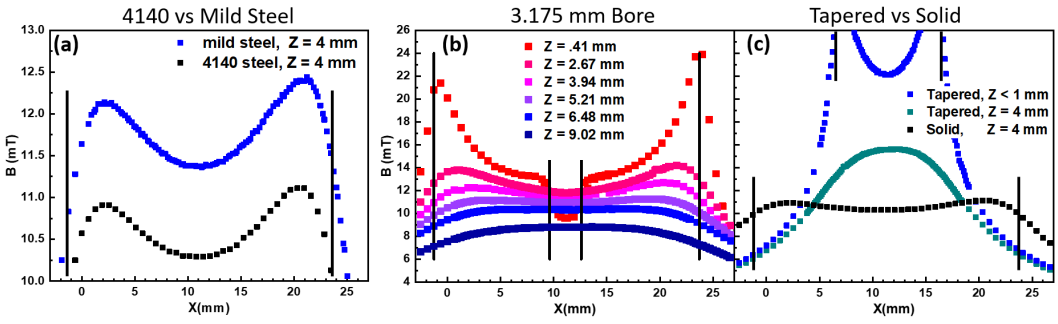

Fig. 13 Magnetic field cross sections from a) 4140 steel vs. mild steel, b) 4140 steel with a 3.175-mm hole, and c) tapered vs. solid electromagnet cores. Vertical lines indicate core edges.

The cores function as expected, generating stronger fields at greater distances from the magnet as compared to air. Mild steel performed approximately 10% better due to its increased iron content than the 4140 steel alloy (Fig. 13). The gradients in the field are also strongest near the magnet and core faces; however, the cross section profiles flatten out at increased distance.

With a bored hole, a distinct drop in the field intensity, approximately 5 mm in diameter, is apparent close to the core face due to the 3.175-mm hole. However, at distances greater than 4 mm from the face, this artifact is no longer apparent (see Figs. 13b and 14). This indicates a desirable region to place the sample for both spatial field homogeneity and increased strength (compared to no core).

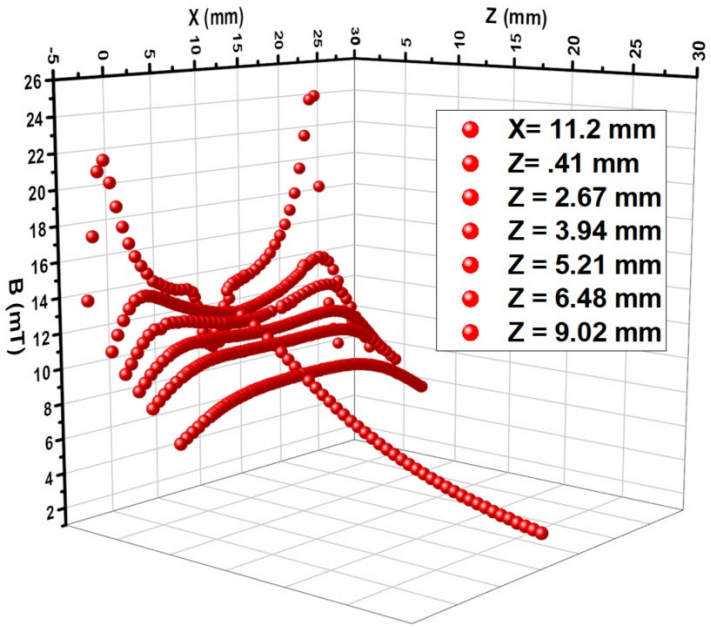

Fig. 14 3-D plot of magnetic field map from 4140 steel core with a 3.175-mm bored hole for laser clearance

The tapered core increased the field roughly 50% over the nontapered core, due to the field being concentrated over a 10-mm-diameter face rather than 25 mm. It also increases inhomogeneity due to the smaller face.

A shock wave will traverse the sample at roughly the sound speed. With a sound speed of 7.18 mm/μs in YIG, the transit time is less than a microsecond, approximately 0.7 μs.[13,14] Thus, detectors with adequate bandwidth to resolve shock demagnetization events need to have a minimum of 1.4 MHz, and more ideally, greater than or equal to 10 MHz of bandwidth (250 MHz would be necessary to observe the shock front actually crossing the 30-μm diode laser spot size). High-speed transimpedance detectors were constructed using PIN photodiodes with nanosecond-scale rise times and are ideal for high-speed detectors. Due to the

strong Faraday rotation resulting in a large amount of light on the detector, it was not necessary to build a more complicated, high-speed amplified circuit. The circuit diagram and detectors are shown in Fig. 15.

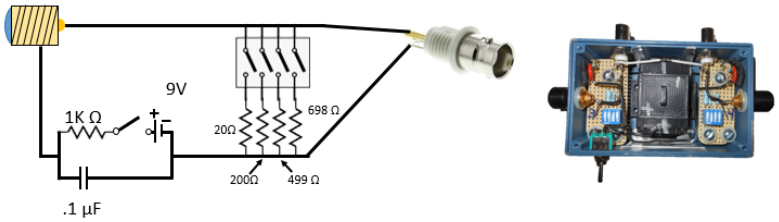

Fig. 15 Circuit diagram and realization of high-speed detectors

Three detectors were built with Si sensors (Thorlabs SM05PD2A). Two of the three also had indium gallium arsenide (Thorlabs SM05PD5A) sensors incorporated, to allow flexibility in probe laser wavelength. The detector bandwidth, f_{BW}, is determined by the photodiode's junction capacitance, C_J, and load resistance, R_L, according to $f_{BW} = \left(2\pi R_L C_J\right)^{-1}$. Applying a reverse bias can further increase the junction capacitance by depleting the semiconductor heterostructure of charge carriers. This bias was increased until the decreasing capacitance no longer improved the response, which occurred at roughly 12 V.

Figure 16 shows the results of characterizing the frequency response of the Si detector, which was done by sinusoidally modulating the output of the 780-nm probe laser from 0–80 MHz. All load resistors showed a broad frequency response, being able to "see" the signal over nearly the entire modulation region. All also showed a strong dip in bandwidth around 28 MHz, at which frequencies the detector is unsuitable. As expected, the induced photocurrent, measured as the voltage over the load resistor, increased with load resistance, though the spectral response became less uniform. A spectrally nonuniform response would distort a spectrally broad signal and this response curve would be necessary for correcting the observed intensity. As the demagnetization signal is expected to be spectrally somewhat narrow, this bandwidth should be acceptable with no spectral corrections necessary.

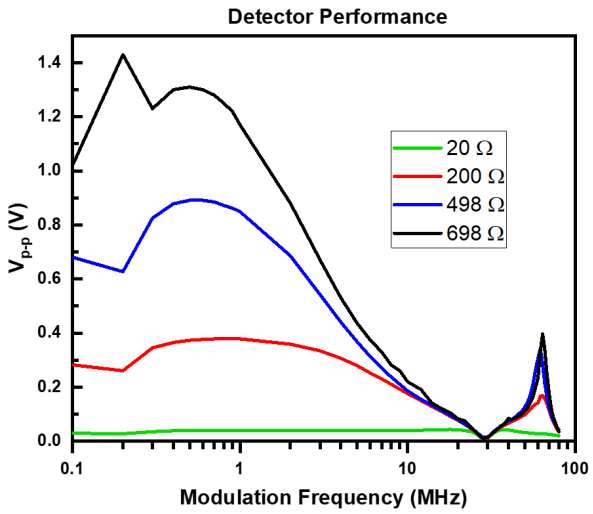

Fig. 16 Observed bandwidth of Si, PIN-diode based detectors as measured by sinusoidally modulating laser input intensity

6. Results

To determine the maximum Faraday rotation exhibited by YIG, the analyzing prism was rotated with respect to the polarizing prism and YIG sample such that the Faraday rotation would minimize (90° in Malus' law) the transmitted light. The advantage of this brute-force method is that it does not require tedious reference measurements (as must be done for a dynamic, shock demagnetization measurement) to use Malus' law to translate the observed intensity into an angle.

Figure 17 shows the probe laser light transmitted through the analyzer, placed at 20° (Fig. 17a) and then 21° (Fig. 17b) away from the polarization angle set by the analyzer, as the external magnetic field is ramped to saturation. Inspecting the low-intensity tails more closely (inset), the 20° detuning in Fig. 17a shows a slight rise starting at 0.10 T, which the 21° detuning in Fig. 17b does not. This indicates the maximum rotation is approximately 21° (600 deg/cm). This measurement also reflects the expected signal-to-noise ratio, about 14 in this case, in a shock demagnetization measurement as the polarizers would be crossed and the applied field would rotate the light transmitted by YIG to this initial angle from which it would fall during demagnetization. If more signal intensity is necessary, a double pass through the sample can be done since unlike waveplates, the Faraday rotation is nonreciprocal and doubles. A 42° angle was confirmed in the same manner as the single-pass configuration.

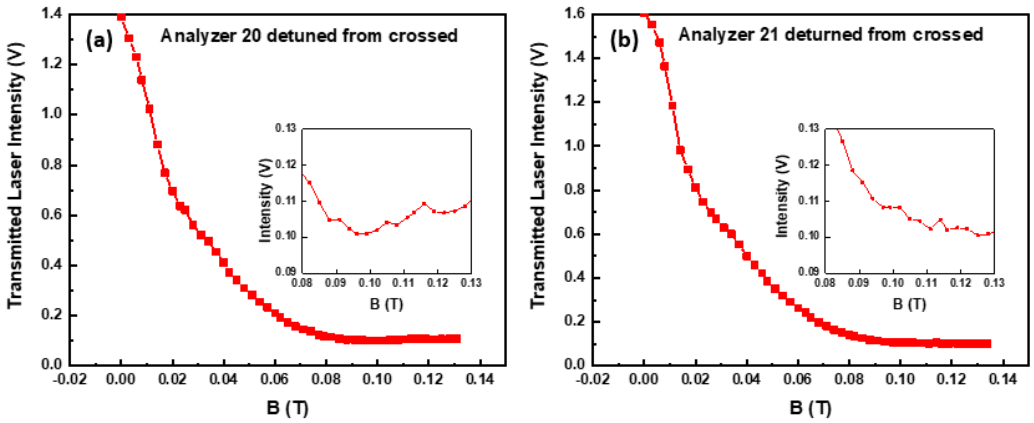

Fig. 17 Probe laser intensity transmitted through the analyzer rotated to a) 20° and b) 21° away from crossed as the applied external field is ramped up. Insets zoomed in on low-intensity tails.

The demagnetization attempts in this work were all done in a low-impulse configuration, with the goal of observing *some* change in the magnetization without destroying the sample. For all measurements, the laser diode was set to maximum intensity at 10 mW. Not only does this generate a signal above the dark current with the polarizers crossed and no applied field (i.e., no Faraday rotation in the sample), it allows for smaller load resistances in the detectors and correspondingly flatter spectral responses.

Figure 18 shows a shock demagnetization attempt. With the magnet field applied, magnetizing the sample, the light intensity before time 0 is due to Faraday rotation (of roughly 15°). At t = 0, the ND:YAG laser fires a single 6-ns pulse focused down into air approximately 10 mm from the sample edge to generate an air shock (i.e., a laser-induced shock wave generated in, and transmitted through, the air). The laser-induced plasma and associated bright broadband emission dominates the signal and decays to near zero after 5 μs. At 18 μs, a dip in the signal intensity was observed and followed by two smaller signals at later times (~37 and 43 μs), possibly resulting from shock reflections within the sample.

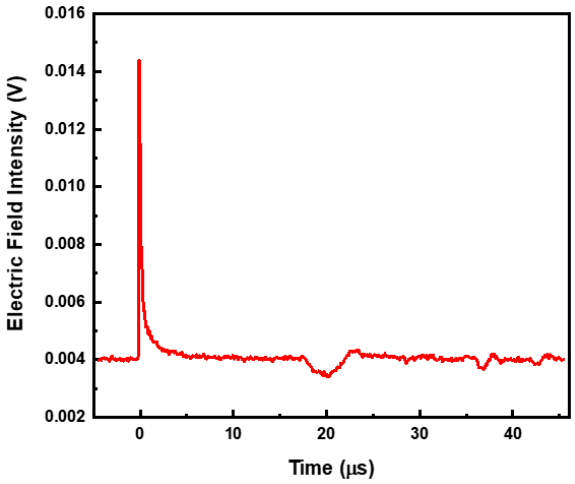

Fig. 18 Signal from YIG in 0.13 T magnetic field and air shock

Examining the validity of this signal motivated the addition of two pickoff detectors, DET1 and DET2 in Fig. 9, to discriminate against nonpolarization-related signals. A commercially available amplified high-speed detector (Newport New Focus 2051 [Newport Corporation, Irvine, California]) was also used to monitor the signal in case the behavior was due to low-intensity noise. Finally, the YIG sample was removed and the shot repeated. Figure 19 shows the result of a shot in air alone, which also shows a dip in the signal. As the laser shock position was varied, the dips tracked accordingly. Upon examining the pickoff detectors, these dips are not due to polarization changes, but rather a change in refractive index of the air due to the air-shock pressure. This change misaligns the beam path into the detectors, decreasing the light coverage on the sensor.

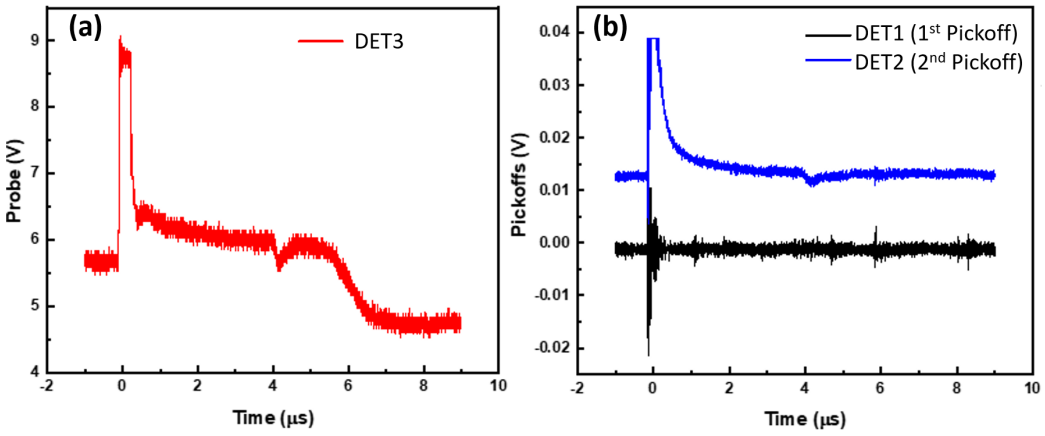

Fig. 19 a) Signal and b) pickoff detector signals during laser-induced breakdown air shock (no sample)

It was found that this effect can be minimized by shielding the beam path with aluminum foil or lens tubes such that only the sample edge is exposed to receive the shock (Fig. 20).

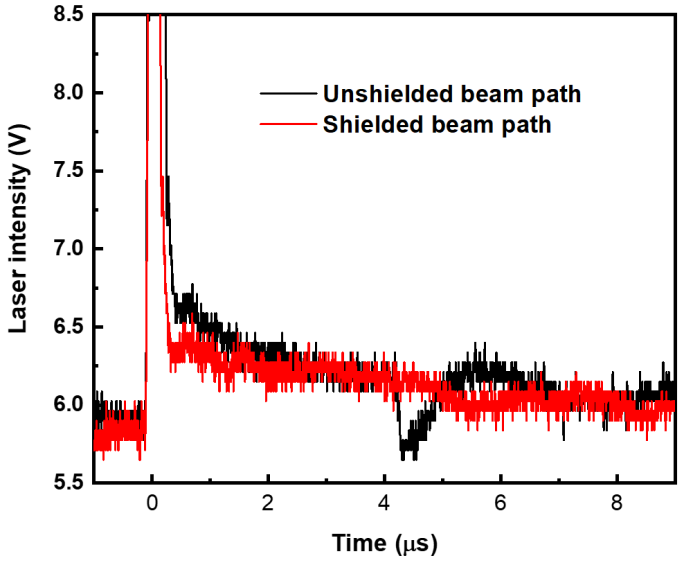

Fig. 20 Effect of shielding the laser-beam path from air-pressure fluctuations generated by laser-induced breakdown in air

In addition to edge-on shocks (which damaged the sample), the focal position of the shock-generating laser pulse was varied to explore the effect on the transmitted shock intensity and period. Face-on placement exacerbated the parasitic refractive index change since the breakdown occurs closest to the path of the probe beamline. Finally, the focus was placed directly on the sample with a drop of super glue on the sample's edge to be vaporized by the intense laser pulse. However, the sustained shock period and intensity were too low to generate a measureable shock anisotropy for demagnetization.

7. Conclusion

Though we were unable to generate sufficiently strong shocks to demagnetize the sample while not destroying it, we have successfully built a high-speed optical magnetization measurement system capable of observing shock demagnetization in real time. Future work will investigate demagnetization using small projectiles to generate the necessary shock (also destroying the samples).

8. References

1. Shkuratov SI, Talantsev EF, Dickens JC, Kristiansen M. Transverse shock wave demagnetization of $Nd_2Fe_{14}B$ high-energy hard ferromagnets. J Appl Phys. 2002;92(1):159–162.
2. Shkuratov SI, Talantsev EF, Dickens JC, Kristiansen M. Compact explosive-driven generator of primary power based on a longitudinal shock wave demagnetization of hard ferri- and ferromagnets. IEEE T Plasma Sci. 2002;30(5):1681–1691.
3. Kulterman RW, Neilson FW, Benedick WB. Pulsed generator based on high shock demagnetization of ferromagnetic material. J Appl Phys. 1958;29(3):500–501.
4. Johnson JH. Theoretical and experimental analysis of the ferromagnetic explosively shocked current pulse generator. J Appl Phys. 1959;30(4):241–243.
5. Grady DE. Shock-induced anisotropy in ferromagnetic material: I. Domain-theory analysis of single-crystal behavior. J Appl Phys. 1972;43(4):1942–1948.
6. Grady DE, Duvall GE, Royce EB. Shock-induced anisotropy in ferromagnetic material: II. Polycrystalline behavior and experimental results for YIG. J Appl Phys. 1972;43(4):1948–1955.
7. Grady DE. Shock-induced magnetic anisotropy in yttrium iron garnet. Arlington (VA): Washington State University/Air Force Office of Scientific Research; 1971. Report No.: AFOSR-TR-71-2570.
8. Wettling W, Andlauer B, Koidl P, Schneider J, Tolksdorf W. Optical absorption and Faraday rotation in yttrium iron garnet. Phys Stat Sol. 1973;59(63):63–69.
9. Dillon JF. Optical absorptions and rotations in the ferrimagnetic garnets. J Phys Radium. 1959;20:374–377.
10. Dorsey PC, Bushnell SE, Seed RG, Vittoria C. Epitaxial yttrium iron garnet films grown by pulsed laser deposition. J Appl Phys. 1993;74(2):1242.
11. Baños-Lopez E, Sanchez-De Jesus F, Cortes-Escobedo CA, Barba-Pingarron A, Bolarin-Miro AM. Enhancement in curie temperature of yttrium iron garnet by doping with neodymium. Materials. 2018;11(9):1652.

12. Wemple SH, Blank SL, Seman JA, Biolsi WA. Optical properties of epitaxial iron garnet thin films. Phys Rev B. 1974;9(5):2134–2144.

13. Clark AE, Strakna RE. Elastic constants of single-crystal YIG. J Appl Phys. 1961;32:1172–1173.

14. Turner E. Interaction of phonons and spin waves in yttrium iron garnet. Phys Rev Lett. July 1960;5(3):100–101.

List of Symbols, Abbreviations, and Acronyms

3-D	three-dimensional
FL	focal length
Nd:YAG	neodymium-doped yttrium aluminum garnet
NIR	near-infrared
Si	silicon
YIG	yttrium iron garnet

1 (PDF) DEFENSE TECHNICAL INFORMATION CTR DTIC OCA

1 (PDF) CCDC ARL
FCDD RLD CL
TECH LIB

37 (PDF) CCDC ARL
FCDD RLW
S SCHOENFELD
FCDD RLW PA
S BILYK
P BERNING
M COPPINGER
J FLENIKEN
M MCNEIR
D MALONE
J NESTA
W UHLIG
L VANDERHOEF
A VALENZUELA
B WILMER
C WOLFE
FCDD RLW B
R BECKER
FCDD RLW PC
J CAZAMIAS
S TURNAGE
C WILLIAMS
FCDD RLW PD
R DONEY
S HALSEY
M KEELE
R MUDD
G VUNNI
M ZELLNER
FCDD RLW C
P BARTKOWSKI
D LYON
FCDD RLW PE
P SWOBODA
FCDD RLW PF
N GNIAZDOWSKI
FCDD RLW B
C HOPPEL
FCDD RLW LB
S DEAN
J GOTTFRIED
K MCNESBY
G SUTHERLAND
FCDD RLW LC
B ROOS
FCDD RLW LE
P WEINACHT
FCDD RLW LH
J NEWILL
J ANGEL
FCDD RLS DP
C TIPTON